

TABLE 1

FITTED PARAMETERS DETERMINED FROM TWO-COMPONENT DECOMPOSITION OF THE LIGHT PROFILES.

Identification IRAS - de Grijp	Morphological Type Hubble	T	μ_{in} (mag arcsec ⁻²)	h_{in} (kpc)	n_{in}	μ_{out} (mag arcsec ⁻²)	h_{out} (kpc)	n_{out}
Warm Seyfert 1								
15015+1037 (359)	E	-5	10.34	3.5E-4	0.25*	24.703	25.24	1.0*
23016+2221 (547)	E1 pec	-5	18.03	2.39	1.31	22.16	8.50	1.0*
13512-3731 (330)	Compact	-3	5.369	6.14E-5	0.25*	20.33	4.58	2.0*
09497-0122 (260)	E/SO	-3	6.63	4.7E-5	0.25	19.936	2.44	2.0*
04124-0803 (114)	SO	-3	5.05	5.7E-5	0.25	21.99	6.41	1.73
05218-1212 (176)	(S?)	0	14.84	0.41	0.69	19.23	3.45	0.73
02366-3101 (55)	S(r)	0	6.90	2.2E-5	0.21	21.62	5.43	0.70
04493-6441 (153)	SO/a	0	17.56	0.97	0.81	22.59	1.03	0.47
21299+0954 (521)	(R)Sa	0	6.66	8.5E-4	0.31	21.12	9.15	1.25
00509+1225 (18)	Sa	1	10.14	0.010	0.38	21.08	10.50	1.34
06563-6529 (213)	Sa	1	...	1.4E-4	0.26	...	3.55	1.36*
11365-3727 (286)	(R')SB(r)	1	...	3.2E-5	0.23	...	1.51	0.81
05136-0012 (171)	Sb pec	2	15.26	0.036	0.34	13.17	0.16	0.74
04339-1028 (139)	SB(s)b pec	3	...	1.4E-4	0.22	...	5.12	1.3
09453+5043 (259)	SB(r)b	3	6.58	8.7E-5	0.25	21.13	8.56	2.0
14557-2830 (358)	Sb	3	...	1.27	1.13	...	9.99	2.0
01378-2230 (31)	Tidal	10	...	0.62	0.72	...	10.99	1.12
Warm Seyfert 2								
04507+0358 (156)	E/SA0-	-4	15.06	0.07	0.39	17.07	0.32	1.03
00521-7054 (19)	E/S0	-3	9.35	3.6E-4	0.26	20.08	1.83	0.60
15304+3017 (375)	S0	-2	16.08	0.18	0.48	26.914	31.25	0.94*
20481-5715 (512)	SA(s)0+	-1	12.98	1.6E-3	0.25	26.79	4.18	1.8
03202-5150 (80)	(R)SB0+	-1	12.11	6.8E-4	0.24	21.29	4.12	2.0*
22017+0319 (528)	SA(s)0+	-1	12.46	8.3E-4	0.24	21.25	1.45	0.64
03355+0104 (96)	S0/a	0	9.73	1.6E-4	0.25	19.61	1.29	0.68
03278-4329 (90)	S0/a	0	...	3.16	0.98	...	2.88	1.45
04229-2528 (122)	S0/a	0	...	1.64	1.88	...	5.23	1.94
11298+5313W (283)	(R')S0/a pec	0	10.29	2.9E-4	0.25	21.78	6.14	1.35
11249-2859 (282)	(R)SB(r)a	1	...	0.03	0.30	...	7.67	1.74
02580-1136 (67)	SAB(rs)a pec	1	11.00	1.4E-5	0.18	17.46	0.04	0.29
13144+4508 (315)	SA(s)a	1	15.23	0.01	0.28	18.41	1.96	1.0*
05238-4602 (179)	Sa tid	1	...	2.75	1.60	...	8.95	1.07
00321-0019 (9)	Sab	2	19.49	1.16	1.59	19.92	7.56	2.09
03059-2309 (72)	SBb pec	3	5.95	4.3E-5	0.25	19.77	5.47	1.04
11298+5313E (283)	SA(s)b	3	15.81	0.57	0.94	19.37	5.75	1.41
08277-0242 (245)	SB(rs)b	3	9.49	1.3E-4	0.24	22.36	13.95	2.0*
03362-1641 (98)	SBb	3	18.72	1.10	1.48	20.14	6.06	1.03
03230-5800 (84)	Sb	3	...	2.74	1.83	...	7.80	1.52
01346-0924 (28)	(R)Sb	3	...	0.75	0.48	...	1.76	1.65
23254+0830 (555)	SA(r)bc pec	4	10.78	4.0E-4	0.26	19.52	4.74	0.85
09182-0750 (253)	SAB(rs)c	5	15.79	0.12	0.52	21.11	7.21	1.78

TABLE 1—*Continued*

Identification IRAS - de Grijp	Morphological Type Hubble	T	μ_{in} (mag arcsec ⁻²)	h_{in} (kpc)	n_{in}	μ_{out} (mag arcsec ⁻²)	h_{out} (kpc)	n_{out}
Cold Sample								
02439-7455	Compact	-5	17.00	0.90	1.21	19.61	1.55	0.70
04454-4838	S0	-2	17.73	0.69	0.75	23.20	6.35	0.87
04015-1118	Sa	1	8.20	9.1E-6	0.19	21.28	5.93	2.0*
23179-6929	SB(s)a	1	17.02	0.48	0.57	23.35	7.39	1.62
05207-2727	(R)SB(s)ab	2	13.45	7.8E-4	0.25	20.050	5.50	1.06
09406+1018N	Sab	2	22.06	11.19	1.82	20.167	3.54	1.40
07514+5327 (231)	SB(rs)b	3	18.25	2.28	1.11	21.09	10.94	1.99
04304-5323	SBb pec	3	18.26	1.94	0.84	23.48	11.97	0.45
06506+5025 (211)	SBc	5	14.15	0.05	0.54	20.10	5.27	2.32**
05217-4245	Sc	5	17.48	0.68	1.05	18.67	4.74	0.99
04265-4801	PR?SB(rl)	5	14.11	1.7E-3	0.25*	23.19	14.69	1.0*
04530-3850	(S?) int	10	17.44	0.90	1.22	19.41	4.34	1.08
03531-4507	Merger	10	16.68	0.19	0.44	25.67	6.61	0.36

*Fixed parameter

**For this object no convergence is achieved for any smaller value of n

This figure "fApp1.jpg" is available in "jpg" format from:

<http://arxiv.org/ps/astro-ph/9912227v1>

TABLE 2
 ELLIPTICITY AND POSITION ANGLE DETERMINED AT a_d .

Identification IRAS - de Grijp	Morphological Type Hubble	T	ϵ	PA (deg)	a_d (kpc)
Warm Seyfert 1					
15015+1037 (359)	E	-5	0.14	-54.35	11.8
23016+2221 (547)	E1 pec	-5	0.15	67.24	6.5
13512-3731 (330)	Compact	-3	0.19	-14.0	4.4
09497-0122 (260)	E/SO	-3	0.25	-18.53	3.0
05218-1212 (176)	(S?)	0	0.26	-12.84	7.7
02366-3101 (55)	S(r)	0	0.03	-66.67	8.6
04493-6441 (153)	SO/a	0	0.23	-88.88	10.4
21299+0954 (521)	(R)Sa	0	0.51	60.70	18.0
00509+1225 (18)	Sa	1	0.05	36.85	5.8
06563-6529 (213)	Sa	1	0.29	-47.52	6.8
11365-3727 (286)	(R')SB(r)	1	0.16	-13.90	3.7
05136-0012 (171)	Sb pec	2	0.17	12.20	6.0
04339-1028 (139)	SB(s)b pec	3	0.60	-1.81	9.0
09453+5043 (259)	SB(r)b	3	0.30	-71.49	9.7
01378-2230 (31)	Tidal	10	0.24	86.74	9.6
Warm Seyfert 2					
04507+0358 (156)	E/SA0 ⁻	-4	0.21	42.90	8.5
00521-7054 (19)	E/S0	-3	0.25	-40.90	3.9
15304+3017 (375)	S0	-2	0.21	-17.26	6.8
20481-5715 (512)	SA(s)0 ⁺	-1	0.19	-59.14	11.0
03202-5150 (80)	(R)SB0 ⁺	-1	0.37	-13.18	8.9
22017+0319 (528)	SA(s)0 ⁺	-1	0.64	0.05	57.58
03355+0104 (96)	S0/a	0	0.46	79.44	7.0
03278-4329 (90)	S0/a	0	0.54	43.70	11.5
04229-2528 (122)	S0/a	0	0.38	-68.30	9.0
11298+5313W (283)	(R')S0/a pec	0	0.41	57.81	6.5
11249-2859 (282)	(R)SB(r)a	1	0.70	-82.50	10.0
02580-1136 (67)	SAB(rs)a pec	1	0.28	11.98	22.0
13144+4508 (315)	SA(s)a	1	0.11	85.48	4.8
05238-4602 (179)	Sa tid	1	0.23	0.0	5.3
00321-0019 (9)	Sab	2	0.73	-19.48	13.0
03059-2309 (72)	SBb pec	3	0.67	84.79	8.7
11298+5313E (283)	SA(s)b	3	0.65	52.40	3.0
08277-0242 (245)	SB(rs)b	3	0.40	-86.60	16.0
03362-1641 (98)	SBb	3	0.56	67.52	5.8
03230-5800 (84)	Sb	3	0.61	66.50	12.0
01346-0924 (28)	(R)Sb	3	0.11	-88.75	5.5
23254+0830 (555)	SA(r)bc pec	4	0.47	-70.07	4.7
09182-0750 (253)	SAB(rs)c	5	0.22	22.29	4.8
Cold Sample					
02439-7455	Compact	-5	0.25	26.33	11.1

TABLE 2—*Continued*

Identification IRAS - de Grijp	Morphological Type Hubble	T	ϵ	PA (deg)	a_d (kpc)
04454-4838	S0	-2	0.24	71.93	4.2
04015-1118	Sa	1	0.26	48.68	6.2
23179-6929	SB(s)a	1	0.49	61.92	4.7
05207-2727	(R)SB(s)ab	2	0.66	41.95	10.0
09406+1018N	Sab	2	0.35	-35.73	6.6
07514+5327 (231)	SB(rs)b	3	0.42	69.48	6.5
10475+1429W	SA(s)b	3	0.79	57.30	8.0
04304-5323	SBb pec	3	0.46	43.92	7.4
06506+5025 (211)	SBc	5	0.57	23.72	5.7
05217-4245	Sc	5	0.62	47.43	7.1
04265-4801	PR?SB(rl)	5	0.14	-21.59	13.7
04530-3850	(S?) int	10	0.57	87.21	4.3
03531-4507	Merger	10	0.37	87.04	10.8
23128-5919 (731)	Merger	10	0.29	-3.58	5.4

This figure "fApp2.jpg" is available in "jpg" format from:

<http://arxiv.org/ps/astro-ph/9912227v1>

Multicolour Optical Imaging of IR-Warm Seyfert Galaxies. III. Surface Photometry: Light Profile Decomposition

Eleni T. Chatzichristou

Leiden Observatory, P.O. Box 9513, 2300 RA Leiden, The Netherlands

NASA/Goddard Space Flight Center, Code 681, Greenbelt, MD 20771

ABSTRACT

This paper is the third in a series, studying the optical properties of a sample of mid-IR Warm Seyfert galaxies and of a control sample of mid-IR Cold galaxies. The present paper is devoted to surface photometry. We analyse the light distributions characterizing the galaxies outside the central 2 kpc. The radial light profiles are decomposed, using two generalized exponentials, in inner and outer components. Each is characterized by the profile shape, central surface brightness and scale length. We find that light is more centrally concentrated in Seyfert 1s, that also tend to lie in earlier-type hosts than Seyfert 2s. Seyfert 1 and 2 bulges have similar shapes but the former are characterized by larger central surface brightnesses and smaller scale lengths. The three parameters characterizing the bulge component correlate with each other, within a limited range of bulge luminosities. Cold galaxies are disk-dominated systems, with complex morphologies. Their bulges are flatter and fainter compared to the Warm sample. The disk structural parameters span similar ranges for the three (sub)samples but with larger scatter. The parametrization of light profiles, as described in this paper, shows that the three (sub)samples occupy different loci in parameter space, that is suggestive of an evolutionary connection between them.

Subject headings: galaxies: active, Seyfert, interactions, photometry

1. Introduction

In the present (third) paper we continue investigating the optical properties of a sample of 54 mid-IR Warm Seyferts selected from the sample of IR-warm IRAS sources of De Grijp et al. (De Grijp et al. 1987 and De Grijp et al. 1992). Our control sample contains 16 mid-IR Cold IRAS galaxies, selected to span similar redshift and luminosity ranges as the Warm sample. In Chatzichristou 2000a (hereafter Paper I) we presented our optical imaging data. In Chatzichristou 2000b (hereafter Paper II) we discussed and intercompared the optical properties of these samples, resulting from our aperture photometry and searched for correlations with their IR properties. In the present third paper we will present, analyse and discuss the results of our surface photometry, performed on most of our sample objects.

This paper is organized as follows: in Section 2 we summarize our method of azimuthal ellipse fitting, two-component decomposition of the projected 1-D light profiles and their parametrization. In Sections 3 and 4 we discuss the various structural parameters characterizing the light distributions and intercompare our Warm and Cold (sub)samples. Our conclusions are summarized in Section 5.

2. Light Profile Decomposition

2.1. Isophotal Fitting

Most of the available isophotal fitting procedures approximate the galaxian isophotes with ellipses at increasing radii and subsequently perform surface and aperture photometry within each ellipse. The basic idea is to sample the image at predefined radii (or rather semi-major axis lengths) along an elliptical path, so that the intensity is the same at all sampling points within the noise. The intensity distribution along the ellipse is fitted by weighted least-squares to an harmonic expression of the type

$$y = y_0 + A_1 \times \sin(PA) + B_1 \times \cos(PA) + A_2 \times \sin(2PA) + B_2 \times \cos(2PA)$$

PA being the position angle; the harmonic amplitudes A_1, B_1, A_2, B_2 parametrize errors in the fitting procedure. Once the best fit ellipse has been obtained, the residuals along this ellipse are parametrized as

$$A_n \times \sin(nPA) + B_n \times \cos(nPA), n = 3, 4$$

These higher harmonic amplitudes A_n, B_n characterize the deviations of a given ellipse from perfect isophotometry. The method is described by Jedrzejewski 1987.

Among available ellipse fitting algorithms we have utilized the WFGAL sub-package of the IRAF/STSDAS applications, which is based upon a combination of tasks that are improved and/or extended versions of the original routines within the ISOPHOTE subpackage. Our method is described in Chatzichristou 1999 and was applied to all of our objects for which either photometric information was available or which possessed well-resolved morphologies.

2.2. Radial Profile Parametrization

Azimuthally averaged profiles have two important advantages over radial (usually along major and minor axes) profiles: first, they allow smoothing of inhomogeneities that could be due to non-uniformly distributed dust, regions of enhanced star formation, or to the presence of non-axisymmetric features and second, they provide improved S/N ratio. The azimuthal averaging can be done without or after deprojection of the galactic disk using an estimation of the galaxy's inclination i . Unless the galaxy shape is simple and well-defined, applying the latter method is subject to uncertainties due to the multiplicity of factors that can affect i , such as, projected dust absorption or real disk distortions.

The effects of seeing (due to Earth's atmosphere and scattering within the telescope) on the intensity and shape parameters of the fitted ellipses can be very important and alter the results in the inner galaxy regions. Although our analysis is mainly concerned with the extended component, we have applied an inner cut-off radius to our surface brightness profiles so that the profile decomposition (described below) is not affected by seeing effects. Usually in such studies the minimum cut-off radius is taken to be half or equal to the seeing PSF, but a more elaborate method is described by Franx et al. 1989. Using their formulae approximated for small core radii and taking $\frac{\Delta I}{I}$ to be equivalent to the error in the local surface brightness due to the seeing effects, we have: $\frac{\Delta I}{I} = \frac{F_2}{r^2}$ where F_2 is the second order moment of the seeing PSF. For our data, we assume a "reasonable" value for $F_2 \simeq 0.8(FWHM)^2$ (see *e.g.*, Franx et al. 1989; Jorgensen et al. 1992. The FWHM for each object is measured on several stars of each image and the mean values are listed in Tables 4 and 5 of Paper I. Requiring that the

error in the local surface brightness be less than 0.10 mag ($\frac{\Delta I}{I} = 0.1$) the inner cut-off radius is determined by $r_{in} = \sqrt{8} \times (FWHM)$. Only in the case of very compact objects, we reduced the cut-off radius to the value of the seeing disk. In any case, the choice of the inner cut-off radius in this study is not crucial, since we are not interested in the detailed structure of the central regions of our galaxies.

Galaxy light profiles are in general more complex than a simple two component model, as indicated by a variety of observational studies. This is due to a variety of factors: (i) The structure (in particular at intermediate radii) can be very complex (*e.g.*, Prieto et al. 1992a and Prieto et al. 1992b), indicating the existence of one or more extra components: bars, rings, lenses (Freeman type II profiles), spiral arms (*e.g.*, Freeman 1977; Freeman 1970; Martin 1995; Serna 1997). The presence of strong star formation in the inner disks mostly affects the *B*-band profiles (for small to intermediate redshift objects). (ii) Dust extinction can affect seriously the observed light distributions, especially at shorter wavelengths (*e.g.*, Disney et al. 1989; Valentijn 1990; White & Keel 1992; Jansen et al. 1994). (iii) Interactions with close companions are often responsible for deformed disks and tidal features, which increase the complexity of the projected light profiles. It is obvious that the use of any simple profile decomposition is bound to have limited success unless one accounts for all the above effects. It is thus often necessary to resort to a one-to-one comparison with the direct images and colour maps, to disentangle the effects of the various components.

The use of a Generalized Exponential Law

Early studies have indeed shown that a simple bulge+disk profile decomposition cannot describe properly more than about half of the observed spiral galaxies (Boroson 1981; Kent 1986). There is accumulated observational evidence that the radial distributions of the spheroidal component of spiral galaxies (bulge) differ significantly from those of ellipticals (*e.g.*, Kormendy & Bruzual 1978; Burstein 1979; Shaw & Gilmore 1989; Kent et al. 1991). Since some ellipticals and disk bulges are well-fitted by the De Vaucouleurs law but there are many that systematically deviate from it, the need for a generalized law with some additional parameter, became obvious. In fact, exponential and generalized exponential laws were successfully used to fit elliptical, S0 and disk galaxy bulge profiles (*e.g.*, Kent et al. 1991; Caon et al. 1993; Andredakis

& Sanders 1994 D’Onofrio et al. 1994; De Jong 1996a; Jerjen & Binggeli 1997). Most of these studies show that exponential bulges are statistically at least as justified as De Vaucouleurs bulges. Independently of the model used for the bulges, an inner disk cut-off is required (Kormendy 1977a) to best fit the light profiles. This agrees with the observed gas distributions of many spiral galaxies. The cut-off could be due to the influence of the gravitational field of a central bar or the fall of material into the galaxy nucleus (*e.g.*, De Vaucouleurs & Freeman 1970). Whether bulge and disk components are physically distinct or not is unclear. Caon et al. 1993 Andredakis et al. 1995 and Jerjen & Binggeli 1997 find a large range of values for the exponent n that describes the shape of the light profiles, consequently, the use of a single law for the description of the profiles of galaxies with a variety of morphological types is clearly inadequate. This is especially true for galaxies with complex morphologies, as is the case for most of our sample objects.

We attempted brightness profile decompositions based on a variety of bulge and disk combinations. First, we defined the bulge and disk dominated regions on the brightness profiles, making also use of the ellipticity and position angle radial profiles: (i) The bulge dominated region should appear linear in the surface brightness vs $r^{1/4}$ plots, starting just outside the radius where seeing effects are important. (ii) The disk-dominated region should be linear in the surface brightness vs radius plots, with ϵ and PA remaining constant all the way out (until the profiles become too noisy or a tidal feature is present). The intermediate transition zone, present in most of our light profiles, was systematically excluded from the fits. We applied a χ^2 polynomial fit to one of the two components, using (i) a De Vaucouleurs $r^{1/4}$ or an exponential law for the bulge and (ii) a simple exponential disk profile. We subtracted the best fit solution from the initial profile and fitted the residual with the second component. This best fit solution was then subtracted from the original profile. The whole process was repeated iteratively until convergence was achieved. For many of our profiles, we repeated the fits starting both from the inner (bulge) and the outer (disk) regions, to check the validity of the results and the uncertainties in the fitted parameters. In general, these were similar for both methods. The best fit results, obtained in this way, provided initial estimates for the spheroidal and disk components and were used to simultaneously fit the two components in the next step. The compos-

ite bulge/disk fitting was done over the whole profile range for relatively simple profiles or, most often, after excluding complex features (bumps and dips) at intermediate radii. The simultaneous two-component fit is based on a non-linear least-squares minimization algorithm to a function of two generalized exponentials. That is, we interactively fitted a function with *six* parameters, using as initial estimates the results from our $r^{1/4}$ +exponential or exponential+exponential fits, above. The form that we have adopted for the generalized exponential is the Sersic profile (Sersic 1968)

$$\Sigma(r) = \Sigma_0 e^{-(\frac{r}{h})^n}, n > 0$$

$\Sigma(r)$ being the surface brightness at radius r , Σ_0 the central surface brightness and h the scale length. The same formula can be written in terms of surface magnitudes

$$\mu(r) = \mu_0 + 1.0857\left(\frac{r}{h}\right)^n$$

(Note that in some studies the power $\frac{1}{n}$ is used instead of n). Smaller values of n lead to more cuspy central light distributions and shallower profiles outwards, while progressively larger values of n will produce flatter central light distributions and truncated outer profiles (see Figure 1). The generalized exponential function includes both the simple exponential case ($n=1$) and the De Vaucouleurs profile using the transformations: $\Sigma_0 = 2138\Sigma_e$, $\mu_0 = \mu_e - 8.325$, $h = 2.89 \times 10^{-4}r_e$ (the subscript e referring to the De Vaucouleurs parameters).

In fact, as shown by Caon et al. 1993, the Sersic formula can be expressed in terms of the radius encircling half of the total luminosity and the corresponding surface brightness. In order to do this, one can express the total luminosity and the surface brightness introducing two coefficients that are functions of the exponent n . Then, for the range of values n that we found, we can compute these coefficients by numerical integration and find two approximate formulas for their dependence on n . We have done this, combining Caon et al. 's and our formulation, which gave to a very good approximation the following transformations between μ , h and μ_e, r_e for our data:

$$\mu_e = \mu_0 + 2.5\left[0.868\frac{1}{n} - 0.142\right]$$

$$r_e = h\left[\frac{2.5\left(0.868\frac{1}{n} - 0.142\right)}{1.0857}\right]^{1/n}$$

We have used the errors in μ (calculated as described in Chatzichristou 1999) for (Gaussian) weighting of the data points, estimating the goodness of fit and calculating errors for the fitted coefficients. Except for cases where the light profiles were relatively simple and the initial parameters well defined, we started by fixing the parameters for the best defined component and allowing the parameters for the second component to vary until a good fit was achieved. Next we kept this set of parameters fixed and varied the other and iterated this process until a good solution was approached. At this point we allowed all six parameters to vary freely and finally calculated the errors for the best fit values. For most objects the fitted range for the exponent n was 0-2, which is the range usually found in previous studies (see discussion in the next section). There were however a few cases of very complex profiles, for which one or both exponents n had to be kept fixed, in order for the fits to converge.

The resulting parameters, that is, the exponent n , the characteristic scale lengths h and the corresponding surface brightness levels μ are tabulated in Table 1, where the subscripts *in* and *out* denote, respectively, the inner (spheroidal) and outer (disk) components. Along with the fitted parameters, we also list in Table 2 the mean ellipticity and position angle estimated at a certain isophotal radius (listed in the same table). Since the outer isophotes for many of our objects are distorted and/or show tidal features (tails or one-sided arms) and strong spiral arms, it is not possible to define a common characteristic brightness level or radius for estimating the disk ellipticities and position angles. Instead, we inspected visually the direct images of all our objects and compared them to the fitted (elliptical) models, in order to find the unaffected isophotes which are mostly located at the edge of the inner disk (avoiding bars and inner rings). Inevitably, the parameters estimated this way are somewhat subjective and should not be used to accurately estimate inclinations for instance, but they *are* indicative of the various subsamples and have a statistical usefulness.

The ellipse fitting procedure, outlined earlier, was applied to all of our objects for which either photometric information was available or which possessed well-resolved morphologies. In the Appendix we present surface brightness and colour profiles for all of them. In a number of cases it was not possible to achieve an accurate decomposition, because of the great complexity of the light distributions (*e.g.*,

most of the mergers). Also we omitted profile decomposition for two objects with photometric information in the Warm sample, because of their small projected sizes. The total numbers of objects with analyzed light profiles, whose parameters are listed in Table 1, are: 17 Seyfert 1s, 23 Seyfert 2s and 14 IR-Cold objects. The parameters obtained from the profile decomposition of objects which have no photometric data, are valid for the scale lengths h and exponents n , but the surface brightness scales were chosen arbitrarily (for the decomposition purpose) and thus are omitted from Table 1 and from all subsequent plots. The information in this table is grouped together for each subsample (Warm Seyfert 1s, Warm Seyfert 2s and Cold galaxies) and, within each subsample, is ranging from early to late type host morphologies. The morphological classification, listed in Table 1, is taken from the literature (when available) and was revised and completed by us, using the revised Hubble classification system and the morphological index T (De Vaucouleurs et al. 1991).

2.3. Light Concentration Indices

A characteristic of galaxy morphologies which is of considerable astrophysical interest, particularly in relation to nuclear activity, is the degree to which light is concentrated towards the central region of the galaxy. There are several parameters which can measure the central concentration. These are based on both the relative importance of the spheroidal component (B) to the disk component (D) and on the ratio of different scale lengths.

(i) Index based on profile decomposition: In the case of a generalized exponential law, we compute the integrated luminosity over the entire galaxian surface to be

$$I_{tot} = \frac{2\pi(1-\epsilon)h^2}{n} \Gamma\left(\frac{2}{n}\right) I_0$$

where $\Gamma(m) = \int_{x=0}^{\infty} e^{-x} x^{m-1} dx$ and $\epsilon = 1 - \frac{b}{a}$ is the ellipticity. The relative importance of the two components is thus given by the ratio

$$C_{I/O} = \frac{I_{tot(in)}}{I_{tot(out)}} = \frac{n_{in}}{n_{out}} \frac{\Gamma\left(\frac{2}{n_{in}}\right)}{\Gamma\left(\frac{2}{n_{out}}\right)} \left(\frac{h_{in}}{h_{out}}\right)^2 10^{-0.4(\mu_{in} - \mu_{out})}$$

the subscripts *in* and *out* referring to the (inner) spheroidal and (outer) disk components, respectively.

We parametrized the light concentration using the following indices:

(ii) Index based on aperture photometry: We can define a similar index to $C_{I/O}$, based on aperture photometry results, this being the ratio of nuclear-to-disk (N/D) or nuclear-to-total (N/T) luminosities (as defined in Paper II). In Table 3 we list $C_{I/O}$, N/D and N/T .

(iii) Indices based on length ratios: These are based on some characteristic radii that are not affected by seeing effects in the inner regions or by sky subtraction uncertainties in the outer regions. Such indices can be defined to characterize the light concentration at various scales and they should all be equivalent (Okamura et al. 1984).

If $L(r) = 2\pi \int_0^r I(r) r dr$ is the luminosity emitted within a radius r and $k(r) = \frac{L(r)}{L_T}$ is the corresponding fraction of the total luminosity L_T , characteristic radii can be defined at: $k(r_{1/5})=0.20$, $k(r_{1/4})=0.25$, $k(r_{1/2})=0.5$, $k(r_{3/4})=0.75$ and $k(r_{4/5})=0.8$. The most commonly used of these ratios is $r_{1/2}$, the radius containing half of the *total* galaxian light (which is analogous to the De Vaucouleurs effective radius r_e for the bulge component).

De Vaucouleurs 1977 defined the concentration index $c_{31} = \frac{r_{3/4}}{r_{1/4}}$. This was found to correlate with morphological type, with c_{31} decreasing from early to late type galaxies. Its theoretical value is 7.0 for a De Vaucouleurs profile and 2.8 for a pure exponential profile.

Kent 1985 has defined the index $c_{42} = \log\left(\frac{r_{4/5}}{r_{1/5}}\right)$, which is equivalent to the Morgan concentration classification scheme (Morgan 1958, Morgan 1959). This index correlates with the $\frac{B}{B+D}$ ratio (for $\frac{B}{B+D} < 0.63$) and with morphological type in the same sense as the c_{31} index. Its theoretical values for a pure $r^{1/4}$ and an exponential profile, are similar to those of c_{31} .

The surface brightness corresponding to the half-light radius $\mu_{1/2}$ shows a tight correlation with c_{42} and c_{31} (Kent 1985; Vitores et al. 1996b), indicating that these parameters describe equally well the galaxian light concentration. The usefulness of $\mu_{1/2}$ as a morphological type indicator is less well defined though, due to the large overlap between different types and its generally large values in the case of emission line galaxies, independently of the host morphologies (Vitores et al. 1996b). The large intrinsic

dispersion in the correlations with Hubble type is a shortcoming in the use of all the above indices (Vitores et al. 1996a).

The surface brightness corresponding to an outermost isophote such as $\mu_{24.5}$ shows no correlation with the above concentration indices or with Hubble type. However, Doi et al. 1993 used it in combination with a new concentration index $c_{in}(\alpha)$ to show that galaxies of different morphological types tend to segregate around different sets of values. In particular, Seyfert type 1 and 2 galaxies are found to be well separated on the $c_{in}(\alpha)$ vs $\mu_{24.5}$ diagram, Seyfert 1s being segregated in the region $c_{in}(\alpha)=0.6-0.7$, $\mu_{24.5}=21.8-22.4$ characteristic of early type galaxies, while Seyfert 2s lie in the region of later type galaxies with large scatter.

We have computed many of the above light concentration indicators; the most useful of them are tabulated in Table 3. In order to calculate concentration indices an estimate of the *total* galaxian light is needed. In Chatzichristou 1999 we describe in detail how our ellipse fitting procedure works, including the calculation of total magnitudes integrating from the outermost fitted isophote to infinity. Here we use these magnitudes to calculate the various characteristic radii and the corresponding indices. In Table 3 we list the concentration parameters $C_{I/O}$, N/D , N/T , c_{31} , the characteristic radius $r_{1/2}$ and the diameter corresponding to the $\mu=25$ mag arcsec $^{-2}$ isophotal level (see Paper II). Note that this table contains more objects than Table 1, because it includes objects for which photometry is available (and thus concentration indices), but no profile decomposition was done.

3. Profile Decomposition: Results and Discussion

We shall now discuss the various structural parameters characterizing the galaxy bulges and disks for our three samples: their distributions, their correlations with each other and with additional observed galaxian properties.

3.1. Concentration Parameters vs Host and Seyfert Types

We shall first consider the distributions of morphological index T (as defined in RC3) and bulge-to-disk ratio, plotted in Figure 2.

3.1.1. Dependence on Morphological Type

In general, a morphological classification is not precise and depends upon the type of data and the classification method used. The uncertainty in index T for two independent classifiers can range from 0.89 (RC3) to 2.2 (Lahav et al. 1995) with an average of 1.5 (De Jong 1996c). Allowing for this uncertainty, which is about half a binsize in Figure 2, we find different trends in the distributions of T for the three subsamples:

Warm Seyfert 1s tend to reside in earlier type hosts compared to Warm Seyfert 2s, although both distributions peak at similar values. This tendency was noticed in a variety of previous studies, where Seyferts were also found to preferentially have spiral or barred spiral morphologies or other kinds of disturbances (*e.g.*, rings) (*e.g.*, Adams 1977, Wehinger & Wyckoff 1977, Simkin et al. 1980, Dahari 1984, MacKenty 1990). In these respects, our IR-Warm Seyferts do not appear to be different than their optically selected counterparts. Our Cold sample galaxies show a clear shift towards later type hosts, although an accurate classification for these objects is difficult given that most are members of closely interacting systems, thus often severely distorted. Consequently, in what follows we denote with $T \geq 10$ the systems with severe distortions, recent mergers or strong tidal features (*e.g.*, one-sided arms) whose main body cannot be classified morphologically.

3.1.2. Dependence on Bulge to Disk Ratio

The index $C_{I/O}$ is, as defined in the previous section, equivalent to the commonly used bulge-to-disk ratio ($\frac{B}{D}$) and its distribution for the various samples is shown in Figure 2. The $C_{I/O}$ distributions of the Warm Seyfert 2 and Cold samples are similar, while the Seyfert 1s show a tail to higher values with a significantly larger median (Table 4). The F-test and Student's t-test however show no statistically significant differences in the variances or means of the three samples. Let us compare our sample's $C_{I/O}$ with that for normal galaxies: A classification scheme established from a sample of field galaxies from the HST Medium Deep Survey through a classical De Vaucouleurs+exponential decomposition (Schmidtke et al. 1997), predicts $1.7 \leq \frac{B}{D} \leq 10$ for bulge-dominated systems, $0.5 \leq \frac{B}{D} \leq 1.7$ for intermediate types (S0s) and $\frac{B}{D} \leq 0.5$ for disk-dominated and pure disk galaxies. (Thus, $C_{I/O}$ larger than 10 in Figure 2, indicate al-

most pure-bulge systems). We caution however that the above values of $\frac{B}{D}$ are uncertain and the error can be as large as 73% of its value (Schmidtke et al. 1997). Even though uncertainties in our $C_{I/O}$ ratio could be of similar magnitude, but the results depicted in Figure 2 are statistically significant and in fact agree with the normal galaxy classification: Seyfert 1s (earlier type hosts) are preferentially bulge-dominated systems while in Seyfert 2 (later type) hosts the disks are predominant. A similar result was reached by us earlier, in Paper II, from aperture photometry when comparing nuclear and disk or total magnitudes.

We plot in the same Figure 2 the distributions of these luminosity ratios, Nuclear/Disk and Nuclear/Total (from Paper II). There is a clear difference between the distributions of Seyfert 1s and Seyfert 2s, this being mainly due to the larger AGN contribution in the former. The K-S test attributes a statistical significance of 99% to the hypothesis that the two distributions are different. On the other hand, there is a striking similarity in the distributions of the Warm Seyfert 2 and Cold galaxies (although at statistical level $<95\%$). The median Nuclear/Total ratio (Table 4) for Seyfert 1s is typical for S0s-S0/a galaxies, for Seyfert 2s characteristic of Sab-Sb types and for the Cold sample is characteristic of Sbc-Sc galaxies (*e.g.*, Kent 1985). While the integrated nuclear magnitudes used in these ratios are dominated by the bright AGN (at least for Seyfert 1s), the bulge component was fitted *excluding* the nuclear (2 kpc) region and thus the $C_{I/O}$ index should be unaffected by the AGN. Consequently, the difference established above between the Seyfert type 1 and 2 host morphological types and light concentration, should not be biased by torus orientation/obscuration effects and thus be an *intrinsic* property of these galaxies.

A correlation between B/D ratio and morphological sequence is suggested by previous studies, although morphological classification and bulge/disk decomposition uncertainties introduce large discrepancies (*e.g.*, Kent 1985, Simien & De Vaucouleurs 1986, Andredakis & Sanders 1994, De Jong 1996c). If true, such a correlation is important because it indicates a common formation process for the galaxy bulges and disks. In Figure 3 we plot Bulge/Disk, Nuclear/Disk and Nuclear/Total ratios against morphological type for all our objects. There is a trend, with large scatter, for these ratios to correlate with host type morphology (particularly in Seyfert 1s) in the expected sense, that is, larger ratios towards ear-

lier type hosts. The scatter in $C_{I/O}$ is particularly large for $T \leq 0$, due to the difficulty in distinguishing real S0s and ellipticals from later-type objects, with low surface brightness disks. The Seyfert 2s and in particular the Cold galaxies show frequently disturbed morphologies and tidal features that lead to uncertain classifications and explain the scatter in the above diagrams. This is the case for some Seyfert 1 galaxies too, for instance IRAS 23016+2221 (the filled circle in Figure 3 with systematically smaller ratios for its assigned morphological type). In the same Figure 3 we indicate the median value of B/D ratio vs morphological type for the sample of face-on spirals of De Jong 1996c (the solid/dashed lines indicate B -band/ K -band data, respectively). Our ratios are computed at an intermediate wavelength (R band) and are consistent on average with these lines.

3.1.3. Dependence on Concentration Parameters

The concentration parameter c_{31} is shown in Figure 4. This index is more likely (compared to $C_{I/O}$) to be affected by the presence of bars, inner rings, or other structures in the “intermediate” zone of light profiles. These features seem to be quite common in our sample galaxies and are likely to introduce large scatter in any existent correlations. This is indeed what we see in Figure 4. It is interesting that Vittores et al. 1996b have similarly found a large range of c_{31} (2.65, 7.21) for their Seyfert sample. We thus conclude that c_{31} is not very useful for objects with disturbed morphologies. The median values, listed in Table 4, are characteristic of S0/a types or earlier for the Seyfert 1 sample, Sa-Sb types for the Seyfert 2 sample and Sbc types or later for the Cold sample.

$r_{1/2}$, the radius within which half of the *total* galaxian light is emitted, shows better discriminating power. In Figure 5 we see a clear difference in the distribution of this parameter between the various samples: Seyfert 1s have smaller $r_{1/2}$ compared to Seyfert 2s and Cold galaxies. This is certainly due to the nucleus dominating the total light of Seyfert 1s. The F-test and Student’s t-test show that the Seyfert 1 and 2 samples have different variances and means at significance levels 0.008 and 6.3E-5, respectively. The K-S test lends statistical significance of $\sim 99.8\%$ that the Seyfert 1 $r_{1/2}$ distribution is different from any of the other two (sub)samples. On the other hand, the Seyfert 1 and Cold galaxy $r_{1/2}$ distributions match at significance level 96% and also have statistically similar variances and means.

We also find a correlation between $r_{1/2}$ and host type T, which is statistically significant only for the Seyfert 2 sample (significance 0.009, with the Spearman's ρ or Kendall's τ rank correlation). However $r_{1/2}$ is also affected by the presence of bars or other central structures, which is the case of the three deviant Seyfert 2s towards larger $r_{1/2}$ values (for their assigned morphological type) in Figure 5. In the same figure we plot the diameters of the $\mu_B=25$ mag arcsec $^{-2}$ isophote, D_{25} , as a function of T. There is an obvious trend for the two quantities to correlate, but with large scatter. The Spearman's rank correlation test shows no correlation at a statistically significant level, for any of the three samples.

The trends/correlations found above between size parameters and morphological type T, suggest that later type hosts tend to have larger scale-lengths *and* sizes. Is this in the sense of the expected linear correlation between $r_{1/2}$ and D_{25} , or does it indicate that late-type hosts tend to be more diffuse (less centrally concentrated)? The r_{12} vs D_{25} plot in Figure 5 shows a correlation between the two quantities (with large scatter) for the three samples. Overplotted are lines of constant ratios between the two scale lengths (the observed median ratio for each sample), roughly indicating the path that points would follow if all galaxies in each sample had similar light profile shapes and μ_0 . Most Seyfert 1s follow such a correlation and this most likely indicates the nuclear dominance of their total light. For Seyfert 2 and Cold galaxies the slope of the relation becomes flatter at large radii/sizes (and thus, as we have shown, later host types). We conclude that the Warm Seyfert 2 and the Cold galaxies have indeed shallower light profiles compared to the Warm Seyfert 1s.

Previous studies have shown that Seyferts are larger than normal spirals or other emission line galaxies. Measured at the 24 mag arcsec $^{-2}$ isophotal level, mean Seyfert diameters are found to be in the range 22.5 kpc (Salzer et al. 1989), 25 ± 10 kpc (MacKenty 1990), or 36 ± 15 kpc (Vitores et al. 1996b). The mean diameters (measured at the 25 mag arcsec $^{-2}$ isophotal level) of our Warm Seyferts are in the same range (see Paper II): 27 (median 25.4) kpc for Seyfert 1s and 33.3 (median 31) kpc for Seyfert 2s. This is also the case for Cold sample objects, mean $D_{25}=30.9$ (median 31.7) kpc, although most of them do not harbour AGN. We conclude that IR-active galaxies tend to be brighter and larger at a given isophote than normal spirals, independently of their nuclear activity stage.

3.1.4. Dependence on Ellipticities

In Figure 6 we show the distribution of ellipticities ϵ for our (sub)samples and also plot the ellipticity as a function of morphological type. The distributions are similarly flat for Seyfert 2s and Cold galaxies, ranging from ~ 0 -0.8, while the range of ellipticities is much narrower for Seyfert 1s, peaking at $\epsilon \approx 0.2$ (see also Table 4). Previous findings that Seyferts have in general ellipticities < 0.5 (Keel 1980, MacKenty 1990, Vitores et al. 1996b) is confirmed only for Seyfert 1s and could be due to these being predominantly face-on systems. However, if the ellipticities presented here are indicative of the galaxy's inclination, their flat distribution would also imply that Seyfert 2s are *not* predominantly edge-on systems but are oriented randomly on the sky. Another possible explanation for the difference in apparent ϵ between our samples is that, if galaxies are thin disks then the ellipticity distribution is expected to be flat, from inclination effects alone. On the other hand, galaxies with strong bulge components would have a distribution of ellipticities peaking around zero. (In this case one would expect to find a well-defined correlation between $C_{I/O}$ and ϵ , which however is not the case.

As we discussed in the previous section, the need to avoid distorted isophotes, that are present predominantly in the Seyfert 2 and Cold samples, introduced non uniformity in the measures of ϵ . It is thus likely that this procedure has introduced the large scatter in ϵ for these two samples.

3.2. Bulges and Disks

3.2.1. Distributions of Characteristic Parameters

In Figure 7 we show the distributions of the bulge (inner) and disk (outer) best fitting parameters, calculated as described in the previous section. We will show that the bulge parameters differ significantly between the three (sub)samples whereas there are less marked differences in their disk properties. More precisely, we find that:

(i) Seyfert 1 bulges have systematically larger central surface brightnesses than Seyfert 2s, although the two subsamples span similar ranges, roughly $\mu_{in}=5$ -20 mag arcsec $^{-2}$. The median μ_{in} values are given in Table 4 and correspond to $\mu_e=17.64$ and 18.77 mag arcsec $^{-2}$, respectively. The Cold galaxies have fainter bulges, with a median μ_{in} equivalent to $\mu_e=19.85$. The F-test shows not significantly different variances

for the three (sub)samples, but the Student’s t-test shows that Cold galaxies have significantly different mean compared to the Seyfert 1 and 2 galaxies (significance 0.001 and 0.01, respectively). The K-S test shows none of the three (sub)samples to have similar distributions.

(ii) The bulge scale lengths span a large range and have similar, flat distributions for the two Seyfert subsamples, but a smaller median for Seyfert 1s (see Table 4). However, the Seyfert 1 bulges have in general steeper profiles (smaller n_{in}), thus the median half light radii (approximated by the relation given in Section 2.2) are similar for the two Seyfert subsamples: $r_e=1.35$ and 1.06 kpc for type 1s and 2s, respectively). There is a bimodal character in the h_{in} distributions for all samples, around values that correspond to $n=0.25$ and 1 , that is, to De Vaucouleurs and simple exponential profiles. Since the simultaneous two component fit was done using initial parameters from two independent bulge and disk fits assuming either an $r^{1/4}$ or r^1 law (see previous section), there might be a best-fit “bias” towards these values in the final results. The Cold sample bulge scale-lengths are shifted to larger values with respect to the Warm samples (equivalent median $r_e=2.14$ kpc) and the variance of its distribution of h_{in} values is significantly different than the Seyfert 1 and 2 subsamples (significance of F-test $3.2E-7$ and $1.4E-5$, respectively).

(iii) There is a marked difference in the distributions of exponents n_{in} between the Warm and Cold samples. Although this parameter spans a remarkably large range for all three samples, Seyfert 1 and 2 galaxies have similar bulge profiles with a median value of $n=0.26-0.30$, that is very close to a De Vaucouleurs $r^{1/4}$ law. The tendency seen in Figure 7 for the Seyfert 1 bulges to be steeper is not confirmed at a statistically significant level. The Cold galaxy bulges are flatter (larger n), with a median $n=0.66$ and a bimodal distribution (around $n_{in}=0.25$ and 1).

(iv) The distributions of the half-light radius r_e and corresponding surface brightness μ_e , show systematic shifts between the three (sub)samples, although less pronounced compared to the h_{in} and μ_{in} distributions. There is no bimodality in the r_e distributions for any of the samples. μ_e is brighter for Seyfert 1s compared to Seyfert 2s and the latter brighter than Cold galaxies. r_e spreads between $\sim 0.1-10$ kpc for the three samples (which are typical values for ellipticals and bulges of disk galaxies), with a peak at ~ 1 kpc for the Warm sample. The Cold sample r_e distribu-

tion is flatter and shifted to larger values compared to the Warm sample.

It is instructive to compare our results for the bulge parameters with previous studies attempting to parametrize spiral galaxy bulges: Profile decompositions using a typical De Vaucouleurs+exponential combination yield median values of $\mu_e=20.8$ mag arcsec $^{-2}$ for S0s and 22.5 mag arcsec $^{-2}$ for Sc types (Kent 1985). A sample of emission line galaxies (Vitores et al. 1996b) shows mean $\mu_e=22.5\pm 1.6$ mag arcsec $^{-2}$, $r_e=2.1$ kpc and $\frac{B}{D}=0.75$. Thus, the Warm Seyfert galaxies have larger characteristic bulge brightness for similar host morphological types. Andredakis et al. 1995 and De Jong 1996b used 2D fitting techniques for their samples of spiral galaxies and applied a generalized exponential to the bulge component in combination with a simple exponential for the disk. They found a large variety of bulge shapes, the parameter n (as defined by us in Section 2) ranging between $\sim 0.2-2$. Jerjen & Binggeli 1997 applied generalized exponentials to ellipticals and found an even larger range for $n \approx 0.08-2.5$. Thus the Warm Seyfert bulges have on average similar profile shapes as normal galaxies for similar morphological types.

(v) In Figure 7 the disk central surface brightnesses show quite similar distributions for the three (sub)samples (mean range of $\mu_{out} \sim 18-24$ mag arcsec $^{-2}$), with similar variances and means. Using the mean disk ($B - R$) colours for each sample from Paper II, we find a range of $\mu_{Bout}=19.1-25.1$ mag arcsec $^{-2}$ for the three samples, with median values 22.01 , 21.24 , 22.35 mag arcsec $^{-2}$ for the Warm Seyfert 1, Seyfert 2 and Cold galaxies, respectively. Given the relatively large errors associated with the fitted parameter μ_{out} (see Table 4), these median values are in agreement with the remarkably uniform, *inclination corrected* central disk brightness first noted by Freeman: $B_0(c) = 21.65 \pm 0.30(\sigma)B\mu$ (Freeman 1970, Boroson 1981, Kent 1985). However, the relatively large range of μ_B that we found for our samples argues against a uniform disk central surface brightness (even allowing for the large errors associated with μ).

The significance of Freeman’s findings about exponential disks has been questioned by various studies since then. Kormendy 1977b showed that the “universal” value of brightness is probably due to selection effects against faint disks and to underestimation of the bulge contribution at outer radii. This conclusion was supported also by later studies (Davies 1990, Phillips & Disney 1993). Indeed, Kormendy fit-

ted the brightness distributions of bulges with a modified Hubble law, and found $B_0(c) = 21.70 \pm 0.23(\sigma)B\mu$ for compact galaxies and $B_0(c) = 22.78B\mu - 22.68B\mu$ for normal galaxies, which is closer to the mean value of our Cold sample. Other explanations have also been put forward for the apparent uniqueness of μ_0 : (a) Selection effects which discriminate against very compact galaxies and galaxies with low surface brightness (De Vaucouleurs 1974, Disney 1976, Allen & Shu 1979). Indeed, Romanishin et al. 1983 found a mean $\mu_0 = 22.74 B \text{ mag arcsec}^{-2}$ for low surface brightness galaxies and Van der Kruit 1987 obtained $\mu_0 = 22.5 B \text{ mag arcsec}^{-2}$ for his sample of spiral galaxies. (b) Dust extinction effects in the B passband (Jura 1980, Valentijn 1990, Peletier et al. 1994). (c) The B passband that Freeman used to establish his relation is dominated by young stars that represent only a few percent of the total stellar mass in a galaxy (De Jong 1996b). De Jong finds that there is no preferred value for the disk central surface brightness of spirals, but only an upper limit and shows that none of the above alternatives *alone* is enough to explain Freeman's law. Yee 1983 found that Seyferts have similar colours and other disk parameters as normal galaxies, but with a tendency for higher central surface brightness ($21.3 B \text{ mag arcsec}^{-2}$) compared to normal spirals. His results agree with ours for the Warm Seyfert 2 sample. MacKenty 1990 found a fainter mean value ($21.9 B \text{ mag arcsec}^{-2}$) for his sample of Seyfert galaxies, which is consistent with the average of our Warm Seyfert sample.

(vi) We find similar disk scale length distributions for the three samples, with a mean range $h_{out} = 1-16$ kpc. The Student's t-test shows no significant difference between the three samples means, but the Seyfert 2 and Cold samples have different variances (significance 0.05 of the F-test). Freeman 1970 found the disk scale lengths to vary between 2 and 10 kpc in S0-Sbc galaxies and between 2 and 5 kpc in Sc-Im galaxies. Similarly, De Jong 1996b found that face-on spirals tend to have disk scale lengths in the range 1-10 kpc. Kormendy 1977b found mean scale lengths 6.5-8.5 kpc for his late type spirals, while Van der Kruit 1987 gives a mean value of only ~ 1.5 kpc for his sample of spirals. For a sample of (mostly late type) emission line galaxies, Vitores et al. 1996b measured $h = 3.2 \pm 2.8$ kpc and Kotilainen & Ward 1994 also found small mean scale lengths ~ 2.5 kpc for their Seyfert sample. We conclude that our IR-selected galaxies have similar median disk scale lengths as nor-

mal spirals, independently of their nuclear activity type (that is, both Warm and Cold samples).

(vii) The disks of our sample galaxies were fitted with a large variety of profiles, $n_{out} \approx 0.6-1.9$ with a median value of 1.3 for the Warm Seyferts and of ~ 1 for the Cold galaxies. Differences between their means or variances are not statistically significant.

3.2.2. Correlations with T and Light Concentration Indices

The question arises whether any (or all) of these parameters are related to the host galaxy morphological type. Let us first briefly summarize the literature on the subject. Kent 1985 applied a classical $r^{1/4}$ bulge + exponential disk decomposition to a galaxy sample covering a large range of morphological types and found that the bulge surface brightness decreases towards later Hubble types (i.e. with decreasing total bulge luminosity). He found (as expected) decreasing $\frac{B}{D}$ or $\frac{B}{T}$ ratios as a function of morphological type, which he showed to be due to decreasing μ_e rather than decreasing bulge size (however, Vitores et al. 1996b finds no evidence for this). De Jong 1996c noticed a similar tight correlation between host morphological type and bulge central surface brightness but not with bulge scale length. Andredakis et al. 1996 and De Jong 1996c applied generalized exponentials to the bulges of spiral galaxies and found a good correlation between n and morphological type (or $\frac{B}{D}$ ratio) in the sense that, S0 bulges resemble an $r^{1/4}$ law, Sa-Sb bulges are best fit with $n=0.5$, while bulges of late type spirals are closer to a simple exponential $n=1$ with possible values as high as $n \sim 2$. Similar correlations for the disk parameters are uncertain: a tendency was found for the central surface brightness to decrease with morphological type, but with large scatter, whereas there is no obvious correlation between disk scale length and morphological type. The apparent lack of correlation between bulge or disk scale lengths and Hubble type, if true, would mean that the Hubble type is scale-free (De Jong 1996c).

We searched for similar correlations in our data but found *no* significant correlation between the bulge or disk parameters and morphological type for any of the samples. Given the uncertainties associated with T (discussed above) this result is not surprising. Thus, we searched for correlations with other light concentration indices. We find a tendency for larger μ_e with light concentration, as expressed by $C_{I/O}$, for Seyfert

1s. There are also correlations between μ_e, r_e and $N/T, N/D$, shown in Figure 8. The scatter is large though and the correlations are better defined for the Cold sample. In addition, the Cold sample μ_e, r_e parameters correlate with host size D_{25} , in the sense of fainter surface brightnesses and larger half light radii for larger hosts. μ_e (calculated outside the central 2 kpc) also correlates with nuclear (within 2 kpc) luminosity for the Cold galaxies. The correlations found above for the Cold sample indicate a smooth distribution of light from the disk to the center, in the absence of an active nucleus, in these objects. The absence of any significant correlation between bulge and nuclear parameters for the Warm Seyfert sample, on the other hand, is a further confirmation that the bulge parameters are not significantly affected by the AGN. We searched for similar correlations for the disk parameters of our objects. We only find a tendency for Seyfert 1 disks to have larger n_{out} (that is, shallower inwards - truncated outwards profiles) in nucleus-dominated objects (larger N/D and N/T ratios) and a tendency for Seyfert 2 bulges to have $n_{in} > 0.25$ only in disk-dominated objects (smaller N/D and N/T ratios). Both these relations are in the expected sense, also found in normal (non-AGN) galaxies.

On the plots of Figure 8 we see clearly the different loci in parameter space that the three (sub)samples occupy: Cold galaxies have fainter μ_e , larger r_e and smaller light concentration indices, the opposite being true for the Warm Seyfert 1 sample. The Warm Seyfert 2 galaxies occupy intermediate loci in these plots, tentatively suggesting a transition between the above two samples. The results outlined so far, indicate significant differences in bulge parameters between the two Seyfert types, which can not be accounted for by the orientation/obscuration unification model (at least in its simplest form, involving the torus orientation).

3.2.3. Inter-Correlations of Bulge and Disk Parameters

In Figure 9 the fitted parameters are plotted against each other, for each of the bulge and disk components. We find some interesting correlations:

(i) The bulge scale length and central surface brightness (upper left panel) show a good correlation with each other, for all three samples. We used the median total bulge luminosity to overplot (solid) lines of constant luminosity for a range of n_{in} values. For

larger total luminosities the lines move parallel and to the right. Two main conclusions can be drawn from this plot: (a) There is a limited range in *total* bulge luminosities. The brightest objects follow the line of constant luminosity for $n_{in}=0.25$ and then move towards larger n_{in} values. This is equivalent to the bimodality in the h_{in} and n_{in} distributions that we found earlier. (b) There seems to be an upper and a lower limit in the (μ_{in}, h_{in}) space: there are no objects with large bulge scale-lengths and high central surface brightnesses or, on the opposite, short scale lengths and low central surface brightnesses, although the latter could be partially due to a selection effect against fainter galaxies. The similar plot for disk parameters (upper right panel) shows some correlation, most of the points lying between the lines of equal luminosity, corresponding to $n_{out}=0.5-1$. One can also define upper and lower limits here, as in the case of bulge parameters.

Although the fitting procedure might contribute to producing such a correlation (*e.g.*, the errors in the fitted parameters might be correlated or the profile fitting might somehow conserve the total bulge flux), this is very unlikely. A similar correlation was noticed in a number of previous studies while applying *different* fitting techniques: Kormendy 1977a found that for the bulges of early type galaxies there is a suggestive correlation between both parameters (μ_e, r_e) and total bulge luminosity. Kent 1985 found a similar correlation of constant luminosity for the *disk* parameters (the same correlation for the bulge seemed looser), the bulges of late type galaxies deviating towards lower luminosities (which was also noted by Andredakis et al. 1995). De Jong 1996c confirmed that the distribution of points in the *disk* (μ, h) plane shows an upper limit that partly follows the line of constant total disk luminosity, while found no correlation in the bulge (μ_e, r_e) plane. All these authors have used different fitting methods and profile models but reached similar correlations. In fact, the correlation between μ_{in}, h_{in} shown here is equivalent to the Fundamental Plane relations, shown in Figure 10 for our samples, using the half-light radius r_e and surface brightness μ_e , derived from the parameters μ_{in}, h_{in} as described in Section 2.

(ii) There is a striking correlation between the bulge scale lengths h_{in} and exponents n_{in} (middle left panel). The solid curves in this plot represent lines of constant total luminosity (the same median value as above) for a range of central surface bright-

nesses. Similar curves for larger total luminosities would move to the right of the plot. The dotted line indicates the index corresponding to a De Vaucouleurs law ($n=0.25$) and the dashed line the simple exponential ($n=0$) case. The observed correlation for the bulge parameters follows the curve corresponding to $\mu_{in}=15$ mag arcsec $^{-2}$ for scale lengths larger than ~ 0.03 kpc. Then, the points move towards larger central surface brightnesses and segregate around $n_{in}=0.25$. This is similar to the result discussed above, that is, that steeper light profiles are needed to accommodate highest central surface brightness bulges. There is significantly larger scatter in the equivalent (n_{out}, h_{out}) diagram for the disk parameters (middle right panel), but most of the points follow here too a curve of constant total luminosity that corresponds to (R band) $\mu_{out} \approx 20$ mag arcsec $^{-2}$ (for the assumed median).

(iii) A correlation between the bulge exponent n_{in} and central surface brightness μ_{in} is implied by correlations (i) and (ii) and is shown in the lower left panel of Figure 9. The scatter increases significantly for $n_{in} \leq 0.4$, the points mostly segregating around $n_{in}=0.25$ (De Vaucouleurs law). The solid curves indicate constant total luminosity (the same median value as in the previous plots) for distinct values of the bulge scale lengths (here again, curves of larger total luminosities move to the right). This plot shows a limited combination of bulge profile shapes and central surface brightnesses, that is, there are no bulges with high μ_{in} and flat profiles or with low μ_{in} and steep profiles. For the equivalent disk parameters n_{out}, μ_{out} (plotted against each other on the lower right panel) there is large scatter and no significant correlation, the points segregating within a relatively narrow range of scale lengths.

Many of the correlations found here were previously noticed for various galaxy samples. In early type galaxies (E, S0 and bright dwarfs), the parameters describing a generalized exponential were found to scale with bulge luminosity, in the sense that brighter galaxies show smaller n and scale lengths h and higher central surface brightness μ (Caon et al. 1993, Jerjen & Binggeli 1997). It was suggested that these relations reflect the dependence of the total light distribution on the underlying total galaxian mass *i.e.*, the depth of the gravitational potential (Young & Currie 1994, Andredakis et al. 1995). Similar n -luminosity and n - h relations were shown to also hold for the bulges of spiral galaxies (Andredakis

et al. 1995, Khosroshani et al. 1999), adding evidence for a similarity between early spiral bulges and (intermediate to low luminosity) ellipticals in terms of projected light distribution (kinematic similarities between the two classes are already known). Finally, good correlations between effective bulge radius and surface brightness or total bulge luminosity are found for bulges of spirals up to Sb types, these being independent of n value, whereas later spiral types were found to systematically deviate from these relations towards lower luminosities, this might be indicating a different formation process for these objects (see also Balcells & Peletier 1994). Within the limited range of bulge luminosities (see above) we find a correlation between μ_e and bulge luminosity only for the Warm Seyfert 1 subsample, while no such correlation is seen for either the Warm Seyfert 2 or the Cold samples. This again argues in favour of intrinsically different bulge properties between the two Seyfert types.

Considering next the disk component, Vitores et al. 1996b find a good correlation between disk scale length and total galaxy luminosity for their sample of emission line galaxies, indicating that these are disk-dominated systems. We searched for correlations between each of the three parameters characterizing the disk component and its total luminosity. There is a large range in the characteristic parameters for a limited range of total luminosities (as seen also from Figure 9), but we find some correlation between μ_{out} and L_{out} , in particular for Seyfert 2s. We find no correlation between any of the disk parameters and the total (broad-band) galaxy luminosities, which is not surprising given the significant contribution of nuclear light to the total luminosities of Seyfert galaxies (in both types) and of additional components such as tidal features to the total luminosities of Cold galaxies (these features were excluded when fitting the disk profiles).

It is interesting to also consider any possible inter-correlations between the equivalent bulge and disk parameters. De Jong 1996c found that using an exponential bulge ($n=1$) an important correlation between r_e and h becomes apparent, not seen when fitting a De Vaucouleurs profile to the bulge. A similar correlation between bulge and disk scale lengths was noticed by Khosroshani et al. 1999 for early type disk galaxies. Such correlations could indicate coupling between the bulge and disk formation in spiral galaxies. We find no significant correlations when using the μ_{in}, h_{in} bulge parameters. However, the half-light equivalent

parameters, μ_e, r_e appear to correlate with μ_{out}, h_{out} for the Cold sample galaxies only. The coupling between bulge and disk confirms our earlier results (Section 3.2.2) for these objects.

4. Conclusions

The main conclusions drawn from the parametrization of the light profiles for our Warm and Cold samples, are as follows:

1. Through different indicators such as morphological classification, Bulge/Disk ratio (from light profile fitting) and relative predominance of the inner component (from concentration indices and aperture photometry) we confirm previous results suggesting that Seyfert 1 nuclei tend to reside in earlier type hosts compared to Seyfert 2s. The IR-Cold galaxies, on the other hand, show complex morphologies and tidal features and are predominantly disk-dominated systems.

2. Most concentration indices fail as indicators of morphological type, due to their sensitivity to the presence of additional features such as bars, rings or tidal extensions. The half-light radius $r_{1/2}$ on the other hand is correlated with host type T and galaxy size. For all our samples we find a correlation between host sizes (larger) and morphological type (later).

3. The Warm Seyfert bulges have similar shapes and their parameters span similar ranges for type 1 and 2 nuclei. However, the former tend to have larger central surface brightness (μ_{in}) and smaller median scale lengths (h_{in}). The IR-Cold galaxies have bulges with fainter μ_{in} , larger h_{in} and flatter shapes (larger n_{in}) compared to the IR-Warm sample. Finally, the Warm Seyfert bulges have overall brighter, while Cold bulges fainter, μ_{in} compared to normal spirals or optically-selected emission line galaxies with similar morphologies.

4. There is a good overlap in the disk properties of our different samples, that is, independently of IR colours and nuclear activity stage. The light profiles have similar shapes, best fit with $n_{out} \geq 0.6$ and the disk scale lengths are similar to those of normal spirals (up to Sbc types). The Warm Seyferts (in particular type 2s) tend to have brighter blue disk surface brightness μ_{Bout} than normal galaxies, while Cold disks are similar to normal galaxy disks. The large range in μ_{Bout} found for our samples argues against a preferred value for this parameter.

5. The complex structure seen for most of our objects (IR Warm and Cold) and the nuclear contamina-

tion, particularly in Seyfert 1s, induce a large scatter in the morphological classification and light concentration indices, thus weakening any existing correlation between them and the bulge or disk parameters. We only find a tendency for bulge-dominated Seyfert 1s to have disks that are flatter inwards and truncated outwards ($n_{out} > 1$) and for disk-dominated Seyfert 2s to have flatter ($n_{in} > 0.25$) bulges.

6. The bulge parameters n_{in} and h_{in} show a bimodal distribution around the values $n_{in}=0.25$ and 1 (that is, the De Vaucouleurs and simple exponential cases), the first better representing high and the latter lower surface brightness bulges. This correlation between μ_{in} and n_{in} indicates a limited combination possible for bulge profile shapes and surface brightnesses: there are no bulges with high μ_{in} and flat shapes or low μ_{in} and steep light profiles. However, these two parameters alone cannot characterize the *total* bulge luminosity, bulges having a variety of scale lengths. We also find that the bulge total luminosities span a narrow range for a variety of (μ_{in}, h_{in}) or (n_{in}, h_{in}) combinations.

7. Disks can have a variety of profile shapes for similar central surface brightness and a limited range of scale lengths. Any correlation between the disk parameters is subject to large scatter, due to the presence of additional components that affect the light profile, but we still find a limited range of total disk luminosities that can be characterized by the (h_{out}, n_{out}) parameters; for a variety of combinations, points tend to cluster around a constant μ_{out} .

8. A last point concerns additional components (bars, rings, spiral or tidal features) that contribute light in excess of the bulge and disk components. In Chatzichristou 1999 we have quantified these, through the definition of an “excess” index and find that this effect is more important for late morphological types and for the more disturbed Warm Seyfert 2 and Cold galaxies.

In the present Paper III, we have shown that the host galaxies of Warm Seyfert types 1 and 2 show significantly different light distributions, at large enough radii (outside the central 2 kpc) that cannot be attributed to any nuclear obscuration effects. Seyfert 1 nuclei tend to reside in bulge dominated hosts, with steeper light profiles (larger light concentration) and smaller sizes (see also Paper II). In Seyfert 2 hosts the light is less centrally concentrated and the bulge component less prominent. In addition, Seyfert 2 hosts tend to have more disturbed morphologies and

overall larger sizes. These differences are suggestive of an evolutionary connection between the two Seyfert types, that might be related to recent interactions/mergers. This suggestion is consistent with our results in Paper II, indicating larger dust content and disk star formation in Seyfert 2 galaxies. In this respect, it is intriguing that the Warm Seyfert 2 properties are intermediate between those of Warm Seyfert 1s and Cold galaxies. The latter reside in late-type hosts of strongly interacting systems, have shallower light profiles and, as their optical and IR colours indicate, are probably dominated by strong disk star formation (Paper II). In Paper V we will further explore the link between the interaction characteristics and the optical properties of our samples and will present evidence for a possible evolutionary scenario. Before this, in Paper IV, we will explore the colour distributions in all our objects and the implications for their stellar content.

I am grateful to my thesis advisors George Miley and Walter Jaffe for providing me with stimulation and support throughout the completion of this project. This research has made use of the NASA/IPAC Extragalactic Database (NED) which is operated by the Jet Propulsion Laboratory, California Institute of Technology, under contract with the National Aeronautics and Space Administration. Part of this work was completed while the author held a National Research Council - NASA GSFC Research Associateship.

REFERENCES

- Adams, T.F. 1977, ApJS, 33, 19
- Allen, R.J., Shu, F.H. 1979, ApJ, 227, 67
- Andredakis, Y.C., Peletier, R.F., Balcells, M. 1996, ASP Conf.Ser., 91, 86
- Andredakis, Y.C., Peletier, R.F., Balcells, M. 1995, MNRAS, 275, 874
- Andredakis, Y.C., Sanders, R.H. 1994, MNRAS, 267, 283
- Balcells, M., Peletier, R.F. 1994, AJ, 107, 135
- Boroson, T. 1981, ApJS, 46, 177
- Burstein, D. 1979, ApJS, 41, 435
- Caon, N., Capaccioli, M., D'Onofrio, M. 1993, MNRAS, 265, 1013
- Chatzichristou, E.T. 2000b, ApJ, *submitted* (Paper II)
- Chatzichristou, E.T. 2000a, ApJ, *submitted* (Paper I)
- Chatzichristou, E.T. 1999, PhD Thesis, Leiden Observatory
- Dahari, O. 1984, PhD Thesis, University of California, Santa Cruz
- Davies, J.J. 1990, MNRAS, 244, 8
- De Grijp, M.H.K., Keel, W.C., Miley, G.K., Goudfrooij, P., Lub, J. 1992, A&AS, 96, 389
- De Grijp, M.H.K., Miley, G.K., Lub, J. 1987, A&AS, 70, 95
- De Jong, R.S. 1996c, A&A, 313, 377
- De Jong, R.S. 1996b, A&A, 313, 45
- De Jong, R.S. 1996a, A&AS, 118, 557
- D'Onofrio, M., Capaccioli, M., Caon, N. 1994, MNRAS, 271, 523
- De Vaucouleurs, G., De Vaucouleurs, A., Corwin, A., Buta, R.J., et al. 1991, Third Reference Catalog of Bright Galaxies, Springer-Verlag, New York
- De Vaucouleurs, G. 1977, in *Evolution of Galaxies and Stellar Populations*, R.B. Larson, Tinsley B.M., Eds., New Haven: Yale Univ. Obs., p.43
- De Vaucouleurs, G. 1974, in *The Formation and Dynamics of Galaxies*, IAU Symp. 58, J.R. Shakeshaft Eds., Reidel, Dordrecht, p.1
- De Vaucouleurs, G., Freeman, K.C. 1970, Vistas in Astronomy, 14, 163
- Disney, M., Davis, J.I., Phillips, S. 1989, MNRAS, 239, 939
- Disney, M.J. 1976, Nature, 263, 573
- Doi, M., Fukugita, M., Okamura, S. 1993, MNRAS, 264, 832
- Franx, M., Illingworth, G., Heckman, T. 1989, AJ, 98, 538

- Freeman, K.C. 1977 in *Structure and properties of nearby galaxies* IAU 77, eds. Berkhuijsen E.M. and Wielebinski R., Reidel, Dordrecht, p.3
- Freeman, K.C. 1970, ApJ, 160, 811
- Jansen, R.A., Knapen, J.H., Beckman, J.E., Peletier, R.F., Hes, R. 1994, MNRAS, 270, 373
- Jedrzejewski, R.I. 1987, MNRAS, 226, 747
- Jerjen, H., Binggeli, B. 1997, in *The Nature of Elliptical Galaxies*, Proceedings of the Second Stromolo Symposium, Eds. M. Arnaboldi, G.S. Da Costa, P. Saha
- Jorgensen, I., Franx, M., Kjaergaard, P. 1992, A&AS, 95, 489
- Jura, M. 1980, ApJ, 238, 499
- Keel, W.C. 1980, AJ, 85, 198
- Kent, S.M., Dame, T., Fazio, G. 1991, ApJ, 378, 131
- Kent, S.M. 1987, AJ, 93, 816
- Kent, S.M. 1986, AJ, 91, 1301
- Kent, S.M. 1985, ApJS, 59, 115
- Kormendy, J., Richstone, D. 1995, ARA&A, 33, 581
- Kormendy, J., Dressler, A., Byun, Y.-I., Faber, S.M., Grillmair, C., et al. 1994, in *ESO/OHP Workshop on Dwarf Galaxies*, Meylan G., Prugniel P. Eds., ESO, Garching, p.147
- Kormendy, J. 1992, in "Galactic Bulges", IAU Symp. 153, Dejonghe H., Habing H., Eds., Kluwer, Dordrecht, p.209
- Kormendy, J., Bruzual, G. 1978, ApJ, 223, L63
- Kormendy, J. 1997b, ApJ, 218, 333
- Kormendy, J. 1997a, ApJ, 214, 359
- Kotilainen, J.K., Ward, M.J. 1994, MNRAS, 266, 953
- Khosroshani, Habib, G., Wadadekar, Yogesh, Kembhavi, Ajit 1999, ApJ, *submitted*
- Lahav, O., Naim, A., Buta, R.J., Corwin, H.G., De Vaucouleurs, G., et al. 1995, Science, 267, 859
- MacKenty, J.W. 1990, ApJS, 72, 231
- Martin, P. 1995, AJ, 109, 2428
- Morgan, W.W. 1959, PASP, 71, 394
- Morgan, W.W. 1958, PASP, 70, 364
- Okamura, S., Kodaira, K., Watanabe, M. 1984, ApJ, 280, 7
- Peletier, R.F., Valentijn, E.A., Morwood, A.F.M., Freudling, W. 1994, A&AS, 108, 621
- Pfenniger, D., Norman, C. 1990, ApJ, 363, 391
- Phillips, S., Disney, M.J. 1993, MNRAS, 203, 55
- Prieto, M., Beckman, J.E., Varela, A.M. 1992b, A&A, 257, 85
- Prieto, M., Longley, D.P.T., Perez, E., Beckman, J.E., Varela, A.M., Cepa, J. 1992a, A&AS, 93, 557
- Romanishin, W., Strom, K.M., Strom, S.E. 1983, ApJS, 53, 105
- Salzer, J.J., MacAlpine, G.M., Boroson, T.A. 1989, ApJS, 70, 479
- Schmidtke, P.C., Windhorst, R.A., Mutz, S.B., Pascarelle, S.M., Franklin, B.E. 1997, AJ, 113, 569
- Serna, A. 1997, A&A, 318, 741
- Sersic, J.L. 1968, Atlas de Galaxias Australes, Observatorio Astronomico, Cordoba
- Shaw, M.A., Gilmore, G. 1989, MNRAS, 237, 903
- Simien, F., De Vaucouleurs, G. 1986, ApJ, 302, 564
- Simkin, S.M., Su, H.J., Schwarz, M.P. 1980, ApJ, 237, 404
- Valentijn, E.A. 1990, Nature, 346, 153
- Van der Kruit, P.C. 1987, A&A, 173, 59
- Vitores, A.G., Zamorano, J., Rego, M., Gallego, J., Alonso, O. 1996b, A&AS, 120, 385
- Vitores, A.G., Zamorano, J., Rego, M., Alonso, O., Gallego, J. 1996a, A&AS, 118, 7
- Wehinger, P.A., Wyckoff, S. 1977, MNRAS, 181, 211
- White, R.E. III, Keel, W.C. 1992, Nature, 359, 129
- Yee, H.K.C. 1983, ApJ, 272, 473
- Young, C.K., Currie, M.J. 1994, MNRAS, 268, L11

TABLE 4
 MEDIAN FITTED QUANTITIES AND ERRORS.

Quantity	Median			σ_{med}
	Seyf 1	Seyf 2	Cold	
μ_{0in} ($\frac{mag}{arcsec^2}$)	8.52	12.462	17.23	0.67
h_{in}^* (kpc)	3.5E-4	0.03	0.58	28%
n_{in}	0.26	0.30	0.66	0.05
μ_{0out} ($\frac{mag}{arcsec^2}$)	21.12	20.08	21.18	1.20
h_{out}^* (kpc)	5.43	5.47	6.14	25%
n_{out}	1.25	1.35	1.07	0.28
ϵ	0.17	0.37	0.42	0.01
$C_{I/O}$	2.14	0.97	0.78	...
N/D	1.36	0.39	0.24	...
N/T	0.58	0.28	0.19	...
C_{31}	5.14	4.33	3.60	...
$r_{1/2}^*$ (kpc)	2.65	4.30	5.30	...

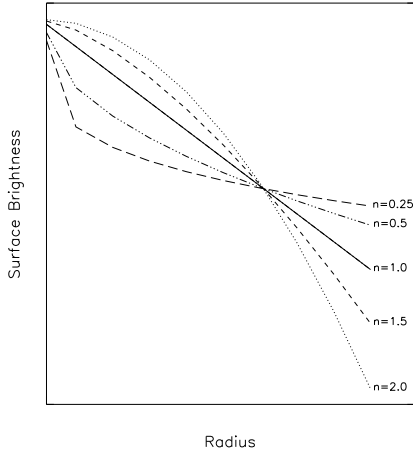


Fig. 1.— The variation in shape of a Sersic (generalized exponential) profile as a function of the exponent value n . The radius where all profiles correspond to the same surface brightness level is the scale length h (arbitrary).

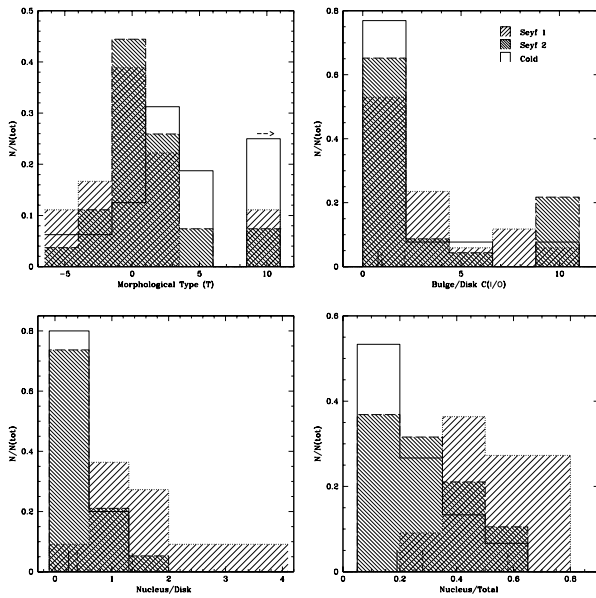


Fig. 2.— Distributions of the morphological types T and the ratios Bulge/Disk (fitted radial profiles), Nuclear/Disk and Nuclear/Total (aperture photometry) for the Warm Seyfert 1 and 2 and the Cold galaxy samples. The vertical bars in the lower x-axes indicate the median values for each sample (also listed in Table 4): short-dashed for Seyfert 1s, long-dashed for Seyfert 2s and solid for the Cold sample.

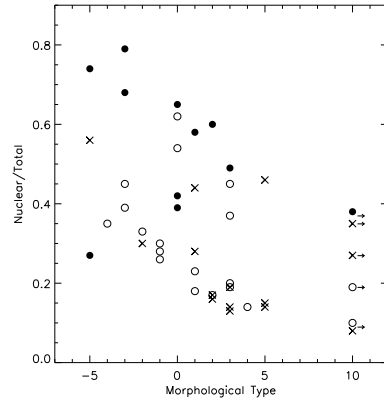
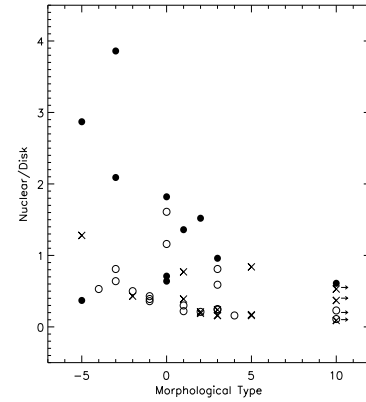
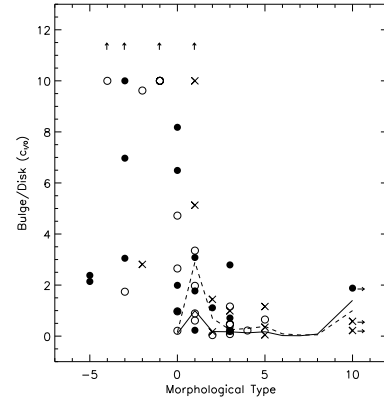


Fig. 3.— The distribution of Bulge/Disk, Nuclear/Disk and Nuclear/Total light ratios as a function of morphological type T . Filled dots represent Seyfert 1s, open dots Seyfert 2s and crosses Cold galaxies. Horizontal arrows indicate $T=10$, arbitrarily assigned to objects with complex or amorphous structures (usually mergers or tidal) while the vertical arrows indicate lower limits for the Bulge/Disk ratios. Overplotted lines indicate median B/D values for a sample of face-on spirals from De Jong 1996c (solid/dashed lines indicate B -band/ K -band data, respectively).

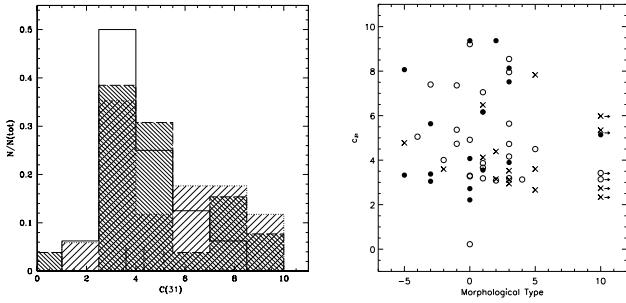


Fig. 4.— Distributions of the concentration index c_{31} for the different samples and as function of morphological type. Symbols are the same as in Figures 2 and 3.

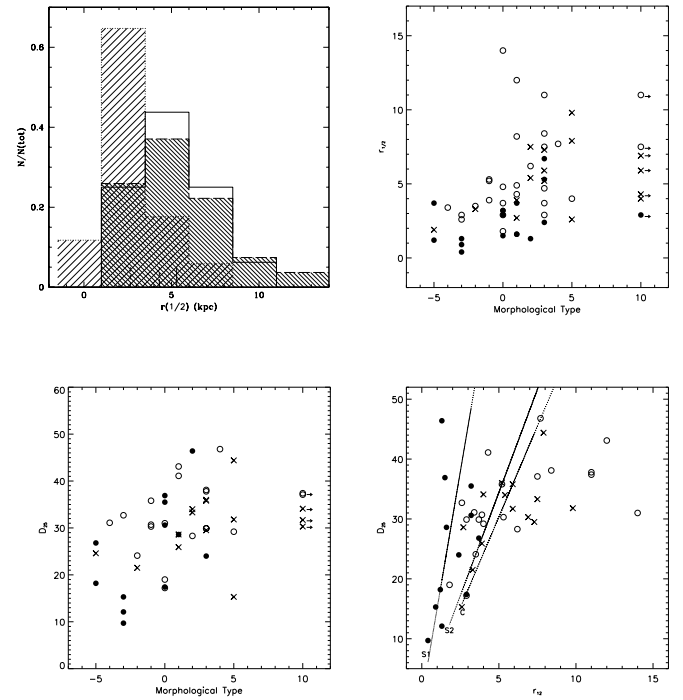


Fig. 5.— Distributions of half-light radii $r_{1/2}$ for the different samples and as function of morphological type (upper panels). Host diameters at $\mu_B=25$ mag arcsec $^{-2}$ as a function of morphological type and the correlation between the two scale lengths (lower panels). Overplotted on the lower right panel are lines of constant ratio between the two scale lengths (the observed median ratio for each sample). Other symbols are the same as in Figures 2 and 3.

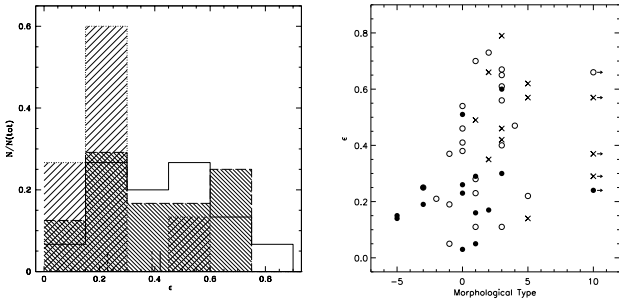


Fig. 6.— The distribution of ellipticities, ϵ , for the three samples and ϵ as a function of morphological type. Symbols are the same as in Figures 2 and 3.

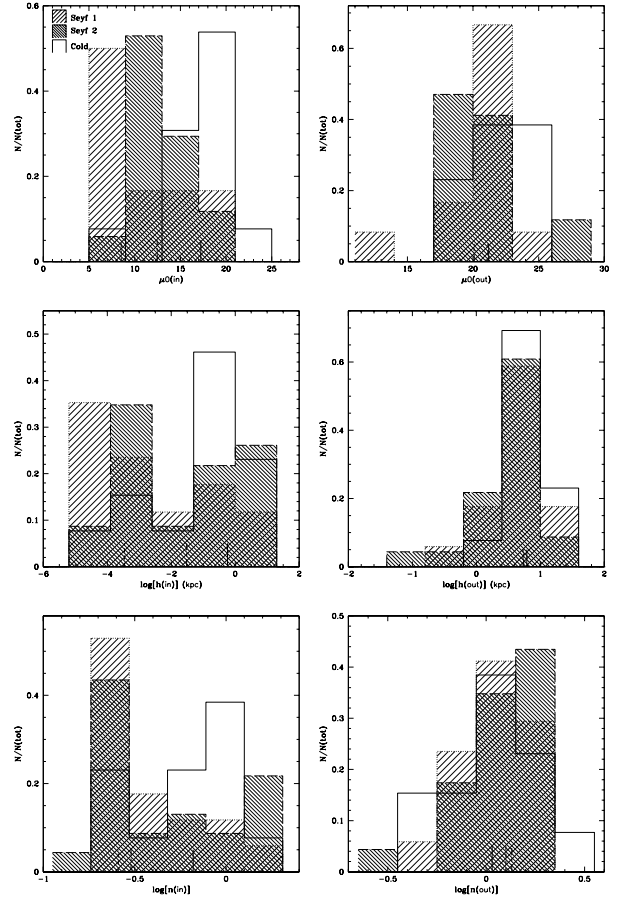


Fig. 7.— The distributions of the fitted parameters of two generalized exponentials, for the bulge(inner) and disk(outer) component, of the radial light profiles. The vertical bars in the lower x-axes indicate the median values for each sample (also listed in Table 4): short-dashed for Seyfert 1s, long-dashed for Seyfert 2s and solid for the Cold sample.

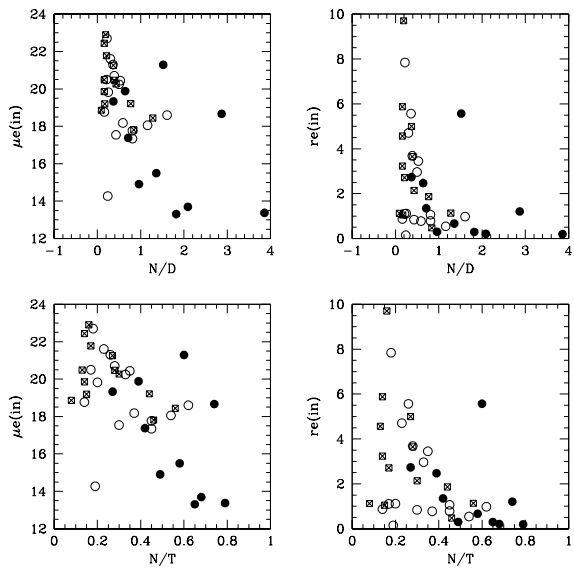


Fig. 8.— Bulge parameters (outside the central 2 kpc) plotted against light concentration indices. Filled/open circles indicate Warm Seyfert types 1 and 2, respectively and crossed triangles represent the Cold sample galaxies.

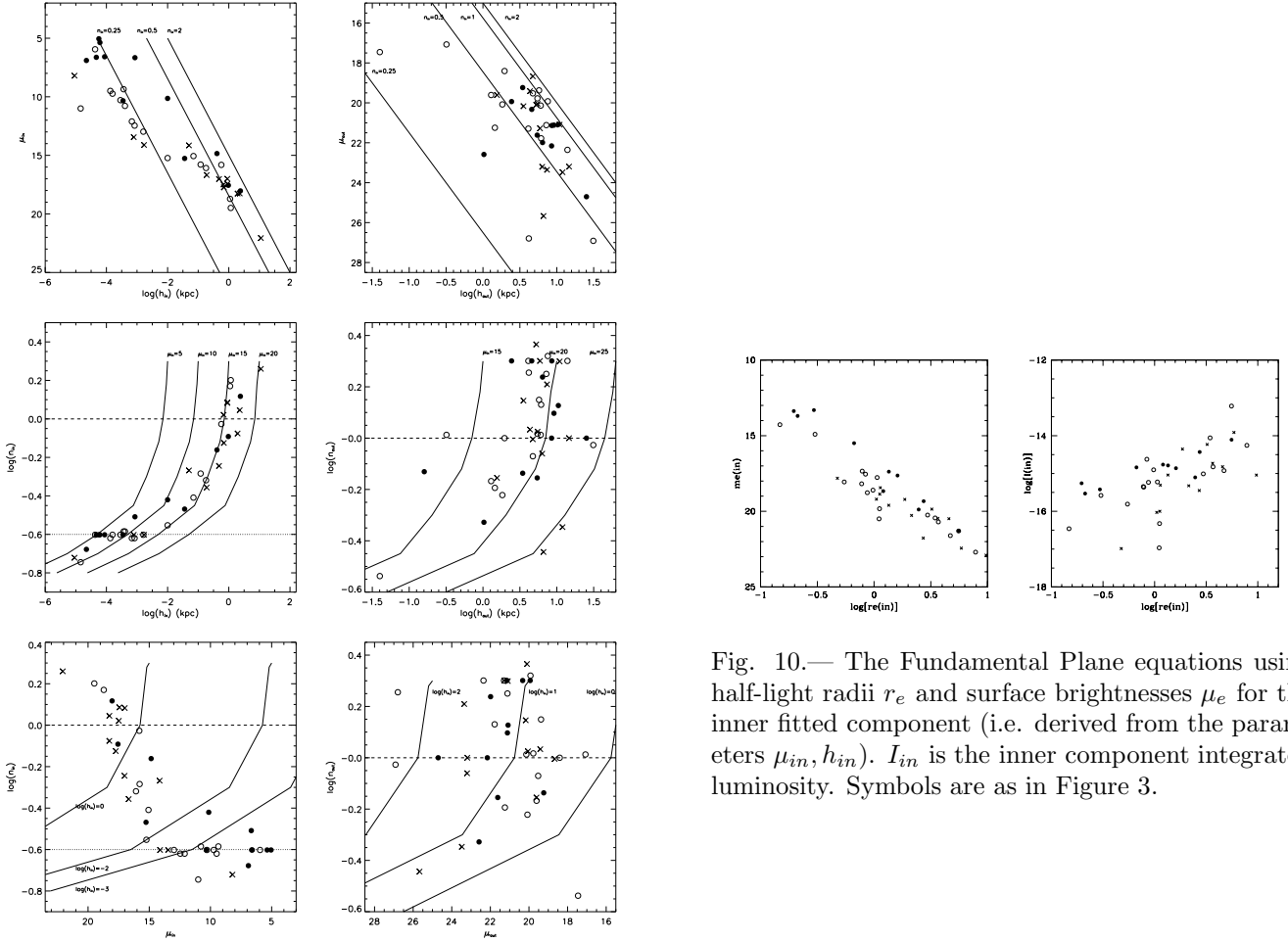


Fig. 9.— Fitted bulge (left panels) and disk (right panels) parameters, plotted against each other. Symbols are as in Figure 3. The full lines indicate constant (bulge or disk) luminosity, the dotted line a De Vaucouleurs ($n=0.25$) and the dashed line a simple exponential law ($n=1$).

Fig. 10.— The Fundamental Plane equations using half-light radii r_e and surface brightnesses μ_e for the inner fitted component (i.e. derived from the parameters μ_{in}, h_{in}). I_{in} is the inner component integrated luminosity. Symbols are as in Figure 3.

Fig. A1.— Warm Seyfert 1: Isolated object with peculiar morphology: elongated nucleus in E-W direction and a tidal-like feature to the SW. Blue nucleus and an horizontal red stripe extending to the E. On the SW a very blue region gives rise to the blue bump at ~ 3 kpc in the colour profiles. The red bump at 6 kpc corresponds to a red feature on the W, probably due to dust extinction. ($B - R$) colour (left) and $H\alpha$ emission (right) maps with size 21×21 kpc. The $H\alpha$ emission is centered on the continuum nucleus (black contours) and appears to be stronger on the E.

Fig. A2.— Warm Seyfert 2: Member of a system of strongly interacting galaxies, exhibiting large tidal tails. Within $\sim 2-8$ kpc the inner disk and a ring-like structure appear as excess light in the surface brightness profiles. At larger radii the knotty spiral arms dominate the light from the object. At ~ 12 kpc a large tidal arm appears on the W side. The red ring structure on the colour map is due to dust, particularly affecting the B image. (The diffuse redder, than the galaxy disk, on the NE end of the colour map is the closest companion galaxy, while the very red spot in the same region is an overlapping star). The spiral arms are composed by bright knots of emission, probably star forming regions, as the $H\alpha$ image is indicating. ($B - R$) (left) and $H\alpha$ (right) maps with size 39.5×39.5 kpc.

Fig. A3.— Cold galaxy: A galaxy with two central knots and complex spiral morphology. The two knots are separated by ~ 1.8 kpc: the southern is redder, embedded in a bar-like structure elongated E-W, and is more likely to be the galactic nucleus, while the northern is diffuse and very blue, probably a giant HII region. The ellipse fits were centered on the S knot, consequently the bump at 1.8 kpc on the surface brightness profiles and blue dip in the colour profiles, are the imprint of the N knot. A bright knotty spiral arm ~ 4.5 kpc to the S, is responsible for the jump on the surface brightness profiles and the blue dip in the colour profiles, in this region. The extended multiple spiral structure appears asymmetric and is composed by bright emission knots. The excess light at ~ 12 kpc in the surface brightness profiles is due to these outer spiral arms, the southern being also the bluer. The $H\alpha$ emission line image shows strong emission associated with the N knot and the 4.5kpc S spiral arm. ($B - R$) colour (left) and $H\alpha$ (right) maps with size 24.6×24.6 kpc. (This object is studied in detail by Chatzichristou et al. , 1998).

TABLE 3
LIGHT CONCENTRATION PARAMETERS.

Identification IRAS - de Grijp	Morphological Type Hubble	T	$C_{I/O}$	N/D	N/T	c_{31}	$r_{1/2}$ (kpc)	D_{25} (kpc)
Warm Seyfert 1								
15015+1037 (359)	E	-5	2.14	2.87	0.74	8.07	1.2	18.2
23016+2221 (547)	E1 pec	-5	2.38	0.37	0.27	3.33	3.7	26.8
13512-3731 (330)	Compact	-3	6.97	2.09	0.68	3.38	1.3	12.1
09497-0122 (260)	E/SO	-3	3.05	5.64	0.4	9.7*
04124-0803 (114)	SO	-3	>10	3.86	0.79	3.05	0.9	15.3
05218-1212 (176)	(S?)	0	0.97	9.37	3.2	30.6*
02366-3101 (55)	S(r)	0	1.99	0.71	0.42	2.21	3.2	35.5
04493-6441 (153)	SO/a	0	8.18	0.64	0.39	2.72	2.9	17.4
21299+0954 (521)	(R)Sa	0	6.49	1.82	0.65	4.07	1.5	36.9
00509+1225 (18)	Sa	1	3.08	1.36	0.58	6.16	1.6	28.6
06563-6529 (213)	Sa	1	1.77	6.17	1.6	...
05136-0012 (171)	Sb pec	2	1.11	1.52	0.60	9.37	1.3	46.4
04339-1028 (139)	SB(s)b pec	3	0.71	7.52	5.3	...
09453+5043 (259)	SB(r)b	3	2.79	0.96	0.49	8.13	2.4	24.0*
14557-2830 (358)	Sb	3	0.21	3.90	6.7	...
11365-3727 (286)	(R')SB(r)	1	0.23	3.55	3.7	...
01378-2230 (31)	Tidal	10	1.88	5.14	2.9	...
19580-1818 (495)	Merger	10	...	0.61	0.38
Warm Seyfert 2								
04507+0358 (156)	E/SA0 ⁻	-4	>10	0.53	0.35	5.05	3.4	31.1
09305-8408 (254)	E/S0 ⁻	-3	...	0.64	0.39	...	2.9	...
00521-7054 (19)	E/S0	-3	1.74	0.81	0.45	7.40	2.6	32.7
15304+3017 (375)	S0	-2	9.62	0.50	0.33	4.01	3.5	24.1*
20481-5715 (512)	SA(s)0 ⁺	-1	>10	0.36	0.26	5.37	5.2	35.8
03202-5150 (80)	(R)SB0 ⁺	-1	>10	0.39	0.28	7.36	5.3	30.3
22017+0319 (528)	SA(s)0 ⁺	-1	10	0.43	0.30	4.73	3.9	30.7*
15599+0206 (392)	S0	0	4.91	14.	31.0**
03355+0104 (96)	S0/a	0	0.97	1.16	0.54	0.22	2.9	17.2
03278-4329 (90)	S0/a	0	4.72	3.27	4.8	...
04229-2528 (122)	S0/a	0	0.21	3.30	3.7	...
11298+5313W (283)	(R')S0/a pec	0	2.65	1.61	0.62	9.21	1.8	19.0
11249-2859 (282)	(R)SB(r)a	1	3.35	3.18	8.2	...
02580-1136 (67)	SAB(rs)a pec	1	0.61	0.22	0.18	3.86	12.	43.1
13144+4508 (315)	SA(s)a	1	1.97	0.30	0.23	3.66	4.3	41.1
05238-4602 (179)	Sa tid	1	0.89	7.05	4.9	...
00321-0019 (9)	Sab	2	0.04	0.21	0.17	3.08	6.2	28.3*
03059-2309 (72)	SBb pec	3	0.45	0.24	0.19	4.16	8.4	38.1
11298+5313E (283)	SA(s)b	3	0.47	0.81	0.45	8.55	2.9	29.9
08277-0242 (245)	SB(rs)b	3	1.16	0.59	0.37	7.95	3.7	29.9*
03362-1641 (98)	SBb	3	0.08	0.25	0.20	4.73	11.	37.8
03230-5800 (84)	Sb	3	0.20	3.19	4.7	...
01346-0924 (28)	(R)Sb	3	0.47	5.64	7.5	...
23254+0830 (555)	SA(r)bc pec	4	0.22	0.16	0.14	3.13	7.7	46.8

TABLE 3—*Continued*

Identification IRAS - de Grijp	Morphological Type Hubble	Type T	$C_{I/O}$	N/D	N/T	c_{31}	$r_{1/2}$ (kpc)	D_{25} (kpc)
09182-0750 (253)	SAB(rs)c	5	0.65	4.50	4.0	29.2*
13536+1836 (333)	Merger	10	...	0.23	0.19	3.42	7.5	37.1
19254-7245 (489)	Merger	10	...	0.11	0.10	3.14	11.0	37.4
Cold Sample								
02439-7455	Compact	-5	1.12	1.28	0.56	4.78	1.9	24.6
04454-4838	S0	-2	2.81	0.43	0.30	3.60	3.3	21.5*
04015-1118	Sa	1	5.13	0.77	0.44	6.48	2.7	28.6
23179-6929	SB(s)a	1	>10	0.39	0.28	4.12	3.9	25.9*
05207-2727	(R)SB(s)ab	2	0.17	0.21	0.17	4.39	7.5	33.3
09406+1018N	Sab	2	1.44	0.19	0.16	3.15	5.4	34.0
07514+5327 (231)	SB(rs)b	3	0.99	0.16	0.14	2.94	5.2	36.0
10475+1429W	SA(s)b	3	...	0.24	0.19	3.12	7.3	29.5
04304-5323	SBb pec	3	0.20	0.16	0.13	3.52	5.9	35.8*
06506+5025 (211)	SBc	5	0.35	0.84	0.46	7.83	2.6	15.3
05217-4245	Sc	5	0.05	0.17	0.15	3.60	7.9	44.4
04265-4801	PR?SB(rl)	5	1.16	0.16	0.14	2.66	9.8	31.8
04530-3850N	(S?) int	10	...	0.09	0.08	2.34	6.9	30.3*
04530-3850S	(S?) int	10	0.22	0.53	0.35	5.98	4.0	34.1*
03531-4507	Merger	10	0.58	0.37	0.27	5.35	5.9	31.7
23128-5919 (731)	Merger	10	2.74	4.3	...

*Diameter of the 25th mag arcsec⁻² isophote measured on the V image

**Diameter of the 25th mag arcsec⁻² isophote taken from literature

This figure "fApp3.jpg" is available in "jpg" format from:

<http://arxiv.org/ps/astro-ph/9912227v1>